Shallow ocean oxygen decline during the end-Triassic mass extinction

Tianchen He[a,*], Robert J. Newton[a], Paul B. Wignall[a], Stephen Reid[a], Jacopo Dal Corso[b],

Satoshi Takahashi[c], Hepin Wu[d], Simona Todaro[e], Pietro Di Stefano[e], Vincenzo Randazzo[f],

Manuel Rigo[g], Alexander M. Dunhill[a]

[a]*School of Earth and Environment, University of Leeds, Leeds LS2 9JT, UK.*

[b]*State Key Laboratory of Biogeology and Environmental Geology, School of Earth Sciences,*

China University of Geosciences, Wuhan 430074, China.

[c]*Department of Earth and Planetary Science, University of Tokyo, Tokyo 113-0033, Japan.*

[d]*State Key Laboratory of Palaeobiology and Stratigraphy & Center for Excellence in Life and*

Paleoenvironment, Nanjing Institute of Geology and Palaeontology, Chinese Academy of

Sciences, Nanjing 210008, China.

[e]*Department of Earth and Marine Sciences, University of Palermo, Palermo 90123, Italy.*

[f]*Earth Sciences Department "Ardito Desio", University of Milan, 20133 Milan, Italy.*

[g]*Department of Geosciences, University of Padova, Padova 35131, Italy.*

* Corresponding author. *E-mail address:* T.He@leeds.ac.uk (T. He).

ABSTRACT

The end-Triassic mass extinction (ETME) was associated with intensified deep-water anoxia in epicontinental seas and mid-depth waters, yet the absolute oxygenation state in the shallow ocean is uncharacterized. Here we report carbonate-associated iodine data from the peritidal Mount Sparagio section (Southern Italy) that documents the ETME (~ 200 Ma) in the western Tethys. We find a sharp drop in carbonate I/(Ca+Mg) ratios across the extinction horizon and persisting into the Early Jurassic. This records local dissolved oxygen and iodate decline in the near-surface ocean of low-latitude Tethys due to the development of depleted oxygen concentrations. Consequently, during the ETME even shallow-water animals, such as the megalodonts seen at Mount Sparagio, were likely the victims of oxygen-poor conditions. The shallow ocean deoxygenation coincides with the synchronous spread of deeper anoxic waters and widespread anoxic deposition on continental shelves and slopes. An upwards expansion of the mid-water oxygen minimum zone in the latest Triassic shoaled the oxycline and triggered a major marine crisis.

Keywords: Shallow ocean deoxygenation; Western Tethys; End-Triassic mass extinction; I/(Ca+Mg)

1. Introduction

Deoxygenation of the upper ocean is a threat to modern marine ecosystems due to global warming and has been observed as a consequence of past warming events at numerous episodes in Earth history (Jenkyns, 2010; Breitburg et al., 2018; Lu et al., 2018; Oschlies, 2021; Song et al., 2021). The end-Triassic mass extinction (ETME; ~200 Ma) is cotemporaneous with a prominent expansion of marine anoxia that is closely linked to the hothouse climate associated with Central Atlantic Magmatic Province (CAMP) volcanism (Ruhl et al., 2011; He et al., 2020). Existing data demonstrate that strengthened anoxic conditions during the ETME were prevalent across many semi-enclosed basins of Europe (Luo et al., 2018; Beith et al., 2021; Fox et al., 2022) and the mid-depth waters of open ocean (Jost et al., 2017; He et al., 2020), whilst the pelagic deeper ocean remained fully-ventilated (Wignall et al., 2010; Fujisaki et al., 2020). Nevertheless, it is largely unknown with respect to the absolute redox state in the upper water column of shallow marine locations across the Triassic–Jurassic (T–J) transition, as the shallow marine ecosystem accounts for the vast majority of aerobic marine organisms and their habitats. Hence, filling this knowledge gap is crucial for tracking the anoxic/hypoxic-extinction link across the ETME.

Carbonate-associated iodine is widely used as a redox proxy to constrain oxic to hypoxic conditions (dissolved oxygen content $[O_2]$ = ~10 to ~100 μmol/kg) in the upper water column (Lu et al., 2010; Hoogakker et al., 2018; Lu et al., 2018; Pohl et al., 2021). The modern ocean has a relatively uniform concentration of iodine due to its long residence time of ~300 kyr. However, the speciation of iodine in the local water column is dependent upon a redox-sensitive pathway between iodate (IO_3^-) and iodide (I^-) (Luther and Campbell, 1991; Rue et al., 1997). Under low oxygen conditions iodate is readily reduced to iodide (Luther and Campbell, 1991; Rue et al., 1997), **and will convert back to its oxidized form** in the presence of abundant dissolved oxygen. **The kinetics of iodide oxidation are slow relative to those of reduction (Chance et al., 2014; Hardisty et al., 2020, 2021)**. Only iodate is readily incorporated into the calcite lattice, substituting for the CO_3^{2-} ion (**Podder et al., 2017; Feng and Redfern, 2018**), which allows the concentrations of this structurally substituted iodine to directly reflect water column redox state during the deposition of carbonate (Lu et al., 2010). Thus, the utilization of I/(Ca+Mg) in ancient carbonates affords an opportunity to trace *in situ* $[O_2]$ variations through time in shallow marine environments. **Because of the slow oxidation kinetics of iodide, the I/(Ca+Mg) proxy can also incorporate a contribution from regional mixing between adjacent water masses (Lu et al., 2020; Hardisty et al., 2021).** Further, carbonate I/(Ca+Mg) can also qualitatively track depth of the oxycline in the water column where the $[O_2]$ decreases more sharply. Carbonate deposited within the shallow ocean realm reflect surface or near-

74 surface seawater dissolved iodate, and is considered to be imparted by the expansion or
75 contraction of a proximal oxygen minimum zone (OMZ) or by fluctuations in the depth of the
76 oxycline (Zhou et al., 2016; Lu et al., 2018).

77

78   Here we present a high-resolution I/(Ca+Mg) record from an upper Rhaetian–lower
79 Hettangian peritidal carbonate succession (Mount Sparagio section, Southern Italy) that was
80 located in the western Tethys (see data in Fig. 1 and Table S1). We show the first evidence of a
81 prominent decline in dissolved oxygen levels in the shallow ocean across the ETME. Low
82 oxygen conditions appear to have persisted into the early Hettangian shallow ocean.

83

84 **2. Palaeogeography and Stratigraphy**
85 The Mount Sparagio (MS) section from western Sicily (Southern Italy) was located at low-
86 latitude of ~15°N in a shallow carbonate platform of the western Tethys (Fig. 1) (Todaro et al.,
87 2017). The studied succession records upper Rhaetian to lower Hettangian peritidal carbonates
88 (Todaro et al., 2017; He et al., 2020). The subtidal facies of Upper Triassic strata are
89 characterized by the occurrence of megalodontids, calcareous algae and a benthic foraminifera
90 association with *Triasina hantkeni*, *Aulotortus* sp., *Auloconus permodiscoides* indicative of a
91 Rhaetian age (Todaro et al., 2017). The extinction horizon is marked by the last occurrence of
92 megalodontids and the characteristic Rhaetian benthic foraminifer *Triasina hantkeni* and occurs
93 immediately below a thin oolitic limestone that is unique to this level at ~200 m height (Fig. 2).
94 **The bloom of the typical Jurassic species** *Thaumatoporella parvovesiculifera* associated with
95 only rare *Aeolisaccus* sp., at a short distance above this oolitic horizon is a further evidence of
96 the extinction interval, and is followed by a slow recovery of the Jurassic benthic community in
97 the earliest Hettangian (Todaro et al., 2018; He et al., 2020).

98

99 **3. Material and methods**
100   A total of 49 well-preserved micritic limestone samples were measured for carbonate-
101 associated iodine concentration. Bulk carbonate rocks were cut into small rock cubes to trim the
102 weathered crust. This was followed by grinding to a fine powder using a TEMA laboratory agate
103 disc mill. Around 20 mg of sample powder was first rinsed by ultrapure water three times and
104 dried. **The protocol of carbonate-associated iodine extraction is a modification after the**
105 **work of Lu et al. (2010).** For each sample approximately 5 mg of cleaned dry powder was then
106 weighed and treated with 3 % (v/v) nitric acid using an ultrasonic bath at room temperature.
107 This carbonate leaching step was completed within 15 minutes to minimize the potential for
108 iodine escape at low pH conditions. The samples were centrifuged and the supernatant
109 containing the leachate was mixed with a 0.5 % (v/v) HNO_3, 0.5 % (v/v) ammonium hydroxide,

110 3 % (v/v) methanol solution. The ammonium hydroxide is required to stabilize the iodine in

111 solution and minimize sample washout times during inductively coupled plasma mass

112 spectrometer (ICP-MS) analysis.

113

114 **Methanol is added to the solution as a source of carbon to promote a signal**

115 **enhancement for iodine measurements. Carbon has been known to enhance the signal for**

116 **iodine on ICP-MS for some time and several studies have systematically investigated this**

117 **effect (Grindlay et al., 2013; Ariga et al., 2019). The effect is not fully understood but is**

118 **attributed to charge transfer reactions occurring in the plasma of the ICP-MS which allow**

119 **difficult to ionize elements such as iodine to be ionized and thus detected by the mass**

120 **spectrometer. Studies have shown that the source of carbon is not important to the effect**

121 **(Grindlay et al., 2013). Methanol was chosen for this work due to its ready availability**

122 **and simplicity to work with. Enhancement of the iodine signal with the addition of carbon**

123 **has been found up to 2.5x that without (Ariga et al., 2019). No increase in background**

124 **signal due to the addition of carbon for iodine was observed in this work.**

125

126 Analysis of these solutions must be complete within 24 hours of dissolution. An aliquot was

127 measured for concentrations of Ca and Mg using a ThermoFisher iCAP 7400 radial inductively

128 coupled plasma optical emission spectrometer (ICP-OES). Samples and calibration standards

129 were internally standardized using 1 mg L^{-1} Y and Lu. A further aliquot was analysed for iodine

130 using a ThermoFisher iCAP Qc ICP-MS in the Aqueous Analytical Facility, University of

131 Leeds. Samples and calibration standards were internally standardized using 5 mg L^{-1} Te and

132 the standards matrixed matched to the samples by addition of 50 mg L^{-1} Ca. The instrumental

133 precisions for Ca, Mg and I are better than 1 %. The ICP-MS was tuned for highest sensitivity

134 to iodine. Repeated measurements of the reference material JCp-1 (coral, *Porites* sp.) yielded a

135 **I/Ca of 4.52 ± 0.14 μmol/mol, which can also be expressed as a** carbonate-associated iodine

136 concentration of 5.48 ± 0.17 μg/g, n=14 (see Table S2 for JCp-1 measurement data), comparable

137 to the published acid-leachable iodine concentration of 5.43 ± 0.07 μg/g, n=8 (Lu et al., 2010)

138 and the certified total measure of iodine concentration of 5.5 ± 0.2 μg/g, n=5 (Chai and

139 Muramatsu, 2007).

140

141 **4. Results and discussions**

142 We first rule out potential lithological and diagenetic controls on the I/(Ca+Mg) dataset **(Table**

143 **S1)**. Samples are dominantly micritic limestone **with uniform CaCO₃ contents mostly above**

144 **90%** and lean in organic matter (He et al., 2020), **suggesting minimal lithological control on**

145 **the variations of I/(Ca+Mg) or contamination by non-carbonate phase** and organic-bounded

146   iodine (Glock et al., 2019). **Mn/Sr ratios in carbonates have been suggested as a measure of**

147   **the degree of post-depositional alteration (Brand and Veizer, 1980) while post-depositional**

148   **dolomitization can be assessed by Mg/Ca ratios.** No correlation is observed with the Mg/Ca

149   or Mn/Sr (Fig. 3), which indicates a minor influence of dolomitization or diagenetic imprint on

150   the structurally incorporated iodine. Hence, the carbonate I/(Ca+Mg) changes at the MS section

151   likely indicate primary signals of water column redox conditions (Lu et al., 2010).

152

153   Our I/(Ca+Mg) profile from MS section documents higher baseline values with an average

154   of **3.5 ± 1.0 µmol/mol (N=32)** throughout the pre-extinction period in the late Rhaetian (Fig.

155   2a). These new I/(Ca+Mg) data add to the existing low-resolution global data compilation for

156   the T–J transition (~200 Ma) (Lu et al., 2018) when seawater iodine concentration depicts a

157   substantial rise from the low plateau phase (~1 µmol/mol) in the Permian–Triassic to high levels

158   (~3 µmol/mol) in the Early Jurassic. Hence, our I/(Ca+Mg) data from MS section validate the

159   previous finding of a long-term increase of oceanic I/Ca ratios from the Triassic to the Jurassic.

160   This change was attributed to a net reduction of oxygen consumption in the upper ocean due to

161   post-ETME radiation of modern-type eukaryotic phytoplankton (Lu et al., 2018).

162

163   Nevertheless, the absolute I/(Ca+Mg) values at MS section fluctuate between 2 µmol/mol

164   and 6 µmol/mol throughout the pre-ETME late Rhaetian (Fig. 2a). This fluctuating I/(Ca+Mg)

165   record may have resulted from a periodic shallowing of the depositional site **as indicated by**

166   **frequent occurrence of red palaeosols (Fig. 2a), which is consistent with facies stacking**

167   **evidence of shallowing-upward cycles (subtidal-intertidal-supratidal) in these peritidal**

168   **sediments (Todaro et al., 2017).** Alternatively, fluctuation in seawater iodine abundance may

169   have been driven by frequent shallowing of water column oxycline that overlies a proximal

170   OMZ, where dissolved iodate were completely reduced to iodide (Zhou et al., 2016; Lu et al.,

171   2018).

172

173   In stark contrast to the pre-extinction interval, I/(Ca+Mg) data record a sharp decline from

174   ~5 µmol/mol to **as low as 0.8 µmol/mol (average of 1.4 ± 0.5 µmol/mol (N=6))** in the latest

175   Rhaetian (Fig. 2a), which coincides precisely with the mass extinction horizon. The extinction

176   is also characterized by the sudden disappearance of megalodont bivalves and the foraminifer

177   *Triasina hantkeni*, and a synchronous positive S-isotope excursion in carbonate-associated

178   sulfate ($\delta^{34}S_{CAS}$; Fig. 2b). Hyperthermal conditions around the T–J transition are thought to have

179   initiated the spread of marine anoxia via increased eutrophication, oxygen consumption and

180   reduction in oxygen solubility in warmer surface waters (He et al., 2020). The large decrease in

181   carbonate I/(Ca+Mg) ratios across the ETME (MS) indicates a depletion of the dissolved iodate

182 pool due to decreased [O$_2$]. The concurrent positive δ^{34}S$_{CAS}$ shift suggests extensive anoxia and

183 burial of pyrite on continental shelves and slopes at this time (He et al., 2020). The spread of

184 anoxic waters would have been enhanced by oceanic sulfate paucity, which would have

185 suppressed the anaerobic oxidation of methane in the sediments, leading to increased benthic

186 methane flux and net oxygen consumption on the seafloor (He et al., 2020). Anoxic conditions

187 likely expanded from the mid-depth OMZ into shallower waters (Fig. 4b), causing hypoxia and

188 iodate depletion in the surface waters. **It is also noteworthy that such correlative redox**

189 **changes through the shallow to mid-depth waters, as demonstrated by coupled I/(Ca+Mg)**

190 **and δ^{34}S$_{CAS}$ trends, are commonly seen in many other prominent anoxic events in the**

191 **geologic past (Lu et al., 2010; Gill et al., 2011; Owens et al., 2017; Edwards et al., 2018).**

192 Thus, the shallowing of the oxycline and upwards invasion of anoxic waters across the ETME

193 is likely to explain the sharp decline in carbonate I/(Ca+Mg) ratios. Indeed, uranium isotope

194 evidence for contemporary deeper water anoxia was found in the adjacent Lombardy Basin (Jost

195 et al., 2017), which likely suggests an upwards expansion of OMZ across the ETME in the area.

196

197 The I/(Ca+Mg) record stays at low level (**1.7 ± 0.4 μmol/mol (N=11)** on average) across the

198 T–J boundary and into the earliest Hettangian (Fig. 2a), indicating continued iodate depletion

199 due to hypoxic conditions in the shallow ocean. However, these post-ETME carbonates exhibit

200 slightly higher iodine concentration compared to those at the major phase of ETME, **associated**

201 **with the recovery of sulfate δ^{34}S (Fig. 2), which may indicate a lesser degree or persistence**

202 **of anoxia/hypoxia.** Further, the uppermost Rhaetian–lower Hettangian sedimentology of the

203 MS section records a minor facies transition to a relatively deeper peritidal setting, evident by

204 the thin oolitic limestone bed at a flooding surface immediately above the extinction horizon

205 and higher occurrence of marly limestone in the lower Hettangian (Fig. 2). Hence, it is possible

206 that MS section saw a transition to slightly deeper facies preceding the ETME, resulting in an

207 improved connection to the open ocean. Thus, the shallow ocean hypoxic condition revealed

208 from the post-extinction MS section likely indicates an open marine signal of dysoxia. These

209 commonly hypoxic conditions likely prevailed in the wider shallow ocean in the post-extinction

210 early Hettangian, possibly with an oscillating redox state as seen in the European epicontinental

211 sea (Beith et al., 2021; Fox et al., 2022). The shallow ocean hypoxia during the T–J transition

212 may have also varied spatially although uranium isotope evidence suggests deeper water column

213 anoxia was widespread until the middle Hettangian Stage (Jost et al., 2017). **Despite low oxygen**

214 **levels in the post-ETME shallow ocean, it did not prolong the extinction or inhibit the local**

215 **recovery of marine communities, although some post-ETME species found at the MS**

216 **section (alga *Thaumatoporella parvovesiculifera* and benthic foraminifers *Siphovalvulina***

217 **sp.) (Todaro et al., 2017, 2018) could be tolerant to oxygen-poor conditions. Furthermore,**

218 **hypoxic conditions in the earliest Hettangian may have had a limited geographic spread**
219 **and likely frequently alternated with periods of oxic water column conditions (He et al.,**
220 **2022), as evidenced by the presence of a diverse benthic fauna in some shallow-water areas**
221 **during the earliest Jurassic (Atkinson and Wignall, 2020; Wignall and Atkinson, 2020).**
222 **Some other environmental stressors for the ETME, such as ocean acidification (Fox et al.,**
223 **2020, 2022), may have receded immediately after the extinction, allowing the shallow**
224 **ocean ecosystem to recover in the early Hettangian.**

225

226   In summary, our new I/(Ca+Mg) record from the MS section in Southern Italy, combined
227 with published $\delta^{34}S_{CAS}$ data provide evidence of oxygen decline in the shallowest realms of
228 western Tethys during the ETME. We attribute this major redox shift to a combined
229 consequence of local $[O_2]$ decrease and possible upwards expansion of oxygen depletion from
230 a mid-depth OMZ to the shallow ocean. The onset of the shallow ocean deoxygenation event
231 was clearly synchronous with the loss of megalodont bivalves and foraminifer *Triasina hantkeni*
232 (Fig. 2), suggesting a cause-and-effect relationship between $[O_2]$ scarcity and ecological stress
233 even in exceptionally shallow-water Tethyan areas. This adds to the growing evidence that
234 indicates a global anoxia/hypoxia-extinction link in a variety of marine settings during the
235 ETME (Jaraula et al., 2013; Jost et al., 2017; Luo et al., 2018; He et al., 2020; Beith et al., 2021;
236 Fox et al., 2022; Kipp and Tissot, 2022). Many similar events through the Mesozoic and
237 Paleogene (e.g., Toarcian oceanic anoxic event, Paleocene-Eocene Thermal Maximum) were
238 accompanied by hyperthermal events and upper ocean hypoxia (Jenkyns, 2010; Lu et al., 2010;
239 Zhou et al., 2014, 2016; Song et al., 2021), which together serve as potential analogues to
240 explore the possible outcomes of ongoing anthropogenic warming.
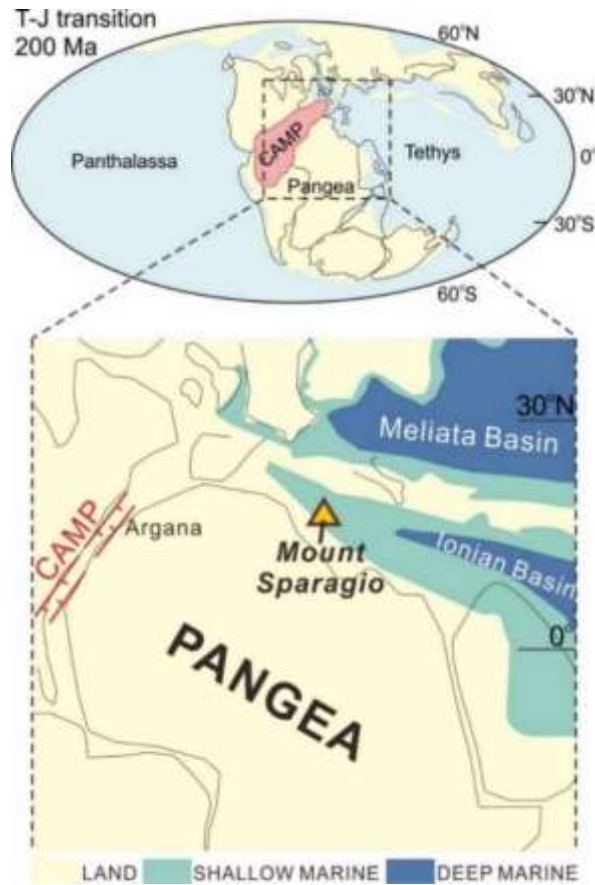
Declaration of competing interest

The authors declare that they have no known competing financial interests or personal relationships that could have appeared to influence the work reported in this paper.

Appendix. Table S1 and S2

Supplementary data to this article can be found at Table S1 and S2.

258

Fig. 1. Paleogeographic map for the shallow marine Mount Sparagio section of western Tethys during the Triassic–Jurassic (T–J) transition. This map is based on Todaro *et al.* (2018). Yellow triangle indicates the location of the studied Mount Sparagio section. CAMP: Central Atlantic Magmatic Province.
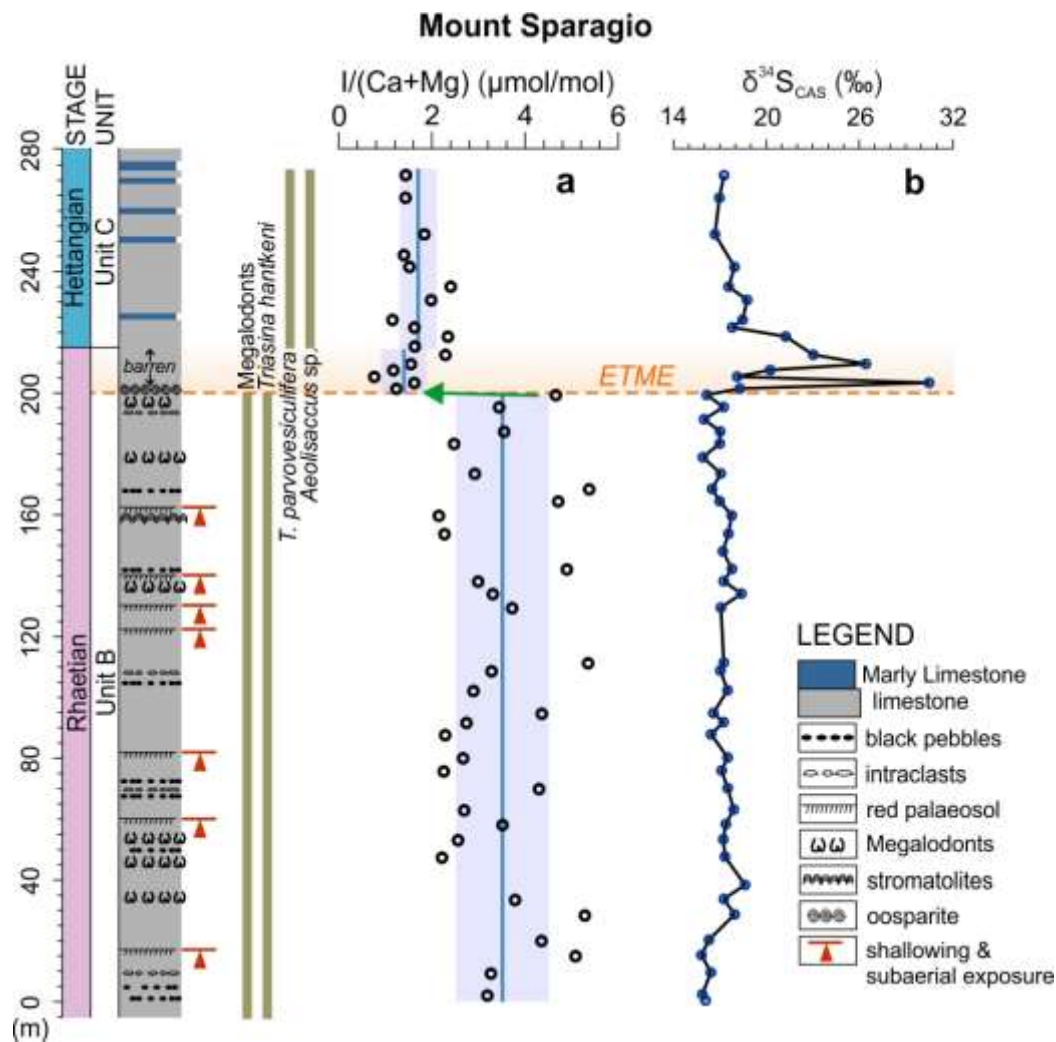
Fig. 2. I/(Ca+Mg) and $\delta^{34}S_{CAS}$ profiles of Mount Sparagio section from Latest Triassic to Early Jurassic. Stratigraphic depth (m) and the lithological log are presented alongside the stages, with stratigraphic units of Todaro *et al.* (2018). Carbonate-associated sulfate $\delta^{34}S_{CAS}$ data are from He *et al.* (2020). The orange horizontal dash line and shadowed field indicate the end-Triassic mass extinction (ETME) at this location. The green arrow indicates the sharp drop in I/(Ca+Mg) across the ETME. **The occurrence of red palaeosols in Unit B indicate subaerial exposure of the site. The vertical blue lines and light purple bands in a show average I/(Ca+Mg) values with uncertainty windows of 1σ standard deviations pre-, during and post-ETME.**

273
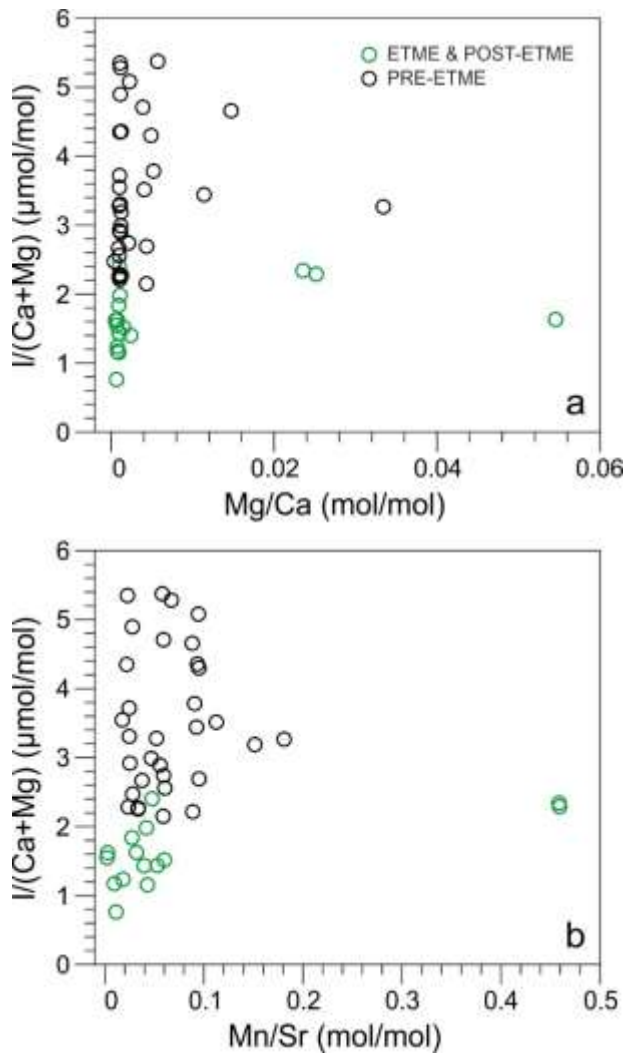
Fig. 3. Correlation between I/(Ca+Mg) molar ratios and elemental mass ratios of carbonates from Mount Sparagio section. **a** Cross-plot of I/[Ca+Mg] and Mg/Ca shows no correlation ($R^2 < 0.001$), suggesting no alteration of redox-proxy values from minor dolomitization (Mg/Ca < 0.06 **mol/mol**). **b** Cross-plot of I/[Ca+Mg] and Mn/Sr displays no correlation ($R^2 = 0.002$), suggesting minimal diagenetic imprint. Mn and Sr data are from He *et al.* (2020). ETME: end-Triassic mass extinction.
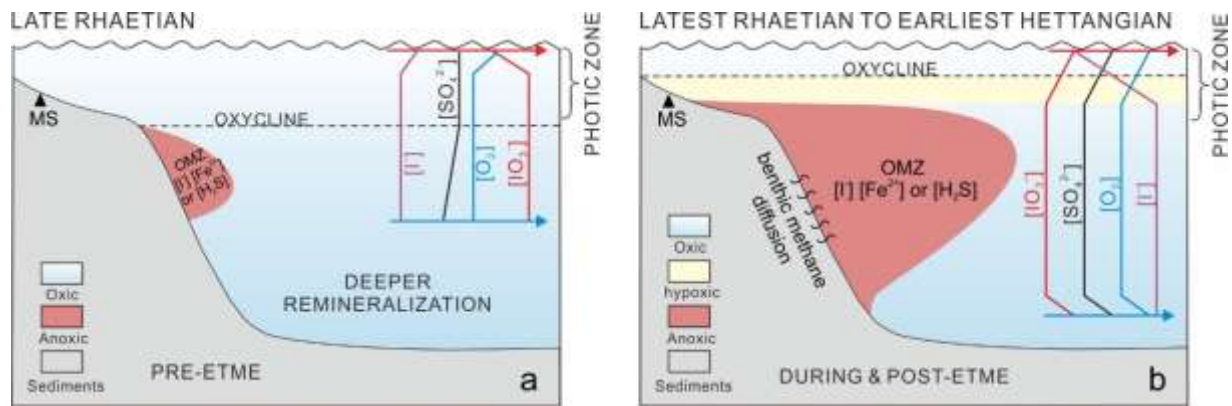
Fig. 4. Schematic diagram of global oceanic redox change through the Triassic–Jurassic transition. Iodine speciation systematics is adapted from Lu *et al.* (2018). Relative concentrations of redox-sensitive elements: iodate (IO_3^-), iodide (I^-) and sulfate (SO_4^{2-}) are indicated. OMZ: Oxygen Minimum Zone. Anoxic-ferruginous and euxinic water column conditions are demarcated with $[Fe^{2+}]$ and $[H_2S]$ respectively. ETME: end-Triassic mass extinction. **a** Pre-ETME 'Mesozoic-type' water column redox state with well-oxygenated upper ocean and restricted OMZ in mid-depth waters. **b** Redox state during and post-ETME showing an expanded OMZ and shallowing of the oxycline, leading to hypoxic conditions and iodate depletion in the shallow ocean. Low sulfate concentration in the ocean likely increased the benthic methane flux to the bottom-water and the oxygen demand (He et al., 2020).

References

Ariga, T., Zhu, Y., Inagaki, K., 2019. Study on carbon-induced signal enhancement in inductively coupled plasma mass spectrometry: an approach from the spatial distribution of analyte signal intensities. J. Anal. At. Spectrom. 34, 1865–1874. https://doi.org/10.1039/C9JA00152B

Atkinson, J.W., Wignall, P.B., 2020. Body size trends and recovery amongst bivalves following the end-Triassic mass extinction. Palaeogeogr. Palaeoclimatol. Palaeoecol. 538, 109453. https://doi.org/10.1016/j.palaeo.2019.109453

Beith, S.J., Fox, C.P., Marshall, J.E.A., Whiteside, J.H., 2021. Recurring photic zone euxinia in the northwest Tethys impinged end-Triassic extinction recovery. Palaeogeogr. Palaeoclimatol. Palaeoecol. 584, 110680. https://doi.org/10.1016/j.palaeo.2021.110680

Brand, U., Veizer, J., 1980. Chemical Diagenesis of a Multicomponent Carbonate System--1: Trace Elements. J. Sediment. Res. 50, 1219–1236. https://doi.org/10.1306/212F7BB7-2B24-11D7-8648000102C1865D

Breitburg, D., Levin, L.A., Oschlies, A., Grégoire, M., Chavez, F.P., Conley, D.J., Garçon, V., Gilbert, D., Gutiérrez, D., Isensee, K., Jacinto, G.S., Limburg, K.E., Montes, I., Naqvi, S.W.A., Pitcher, G.C., Rabalais, N.N., Roman, M.R., Rose, K.A., Seibel, B.A., Telszewski, M., Yasuhara, M., Zhang, J., 2018. Declining oxygen in the global ocean and coastal waters. Science. 359. https://doi.org/10.1126/science.aam7240

Chai, J.Y., Muramatsu, Y., 2007. Determination of Bromine and Iodine in Twenty-three Geochemical Reference Materials by ICP-MS. Geostand. Geoanalytical Res. 31, 143–150. https://doi.org/10.1111/j.1751-908X.2007.00856.x

Chance, R., Baker, A.R., Carpenter, L., Jickells, T.D., 2014. The distribution of iodide at the sea surface. Environ. Sci. Process. Impacts 16, 1841–1859. https://doi.org/10.1039/c4em00139g

Edwards, C.T., Fike, D.A., Saltzman, M.R., Lu, W., Lu, Z., 2018. Evidence for local and global redox conditions at an Early Ordovician (Tremadocian) mass extinction. Earth Planet. Sci. Lett. 481, 125–135. https://doi.org/10.1016/j.epsl.2017.10.002

Feng, X., Redfern, S.A.T., 2018. Iodate in calcite, aragonite and vaterite CaCO3: Insights from first-principles calculations and implications for the I/Ca geochemical proxy. Geochim. Cosmochim. Acta 236, 351–360. https://doi.org/10.1016/j.gca.2018.02.017

Fox, C.P., Cui, X., Whiteside, J.H., Olsen, P.E., Summons, R.E., Grice, K., 2020. Molecular and isotopic evidence reveals the end-Triassic carbon isotope excursion is not from massive exogenous light carbon. Proc. Natl. Acad. Sci. U. S. A. 117, 30171–30178. https://doi.org/10.1073/pnas.1917661117

Fox, C.P., Whiteside, J.H., Olsen, P.E., Cui, X., Summons, R.E., Idiz, E., Grice, K., 2022.

328 Two-pronged kill mechanism at the end-Triassic mass extinction. Geology.

329 https://doi.org/10.1130/G49560.1

330 Fujisaki, W., Fukami, Y., Matsui, Y., Sato, T., Sawaki, Y., Suzuki, K., 2020. Redox

331 conditions and nitrogen cycling during the Triassic-Jurassic transition: A new perspective

332 from the mid-Panthalassa. Earth-Science Rev. 204, 103173.

333 https://doi.org/10.1016/j.earscirev.2020.103173

334 Gill, B.C., Lyons, T.W., Jenkyns, H.C., 2011. A global perturbation to the sulfur cycle during

335 the Toarcian Oceanic Anoxic Event. Earth Planet. Sci. Lett. 312, 484–496.

336 https://doi.org/10.1016/j.epsl.2011.10.030

337 Glock, N., Liebetrau, V., Vogts, A., Eisenhauer, A., 2019. Organic heterogeneities in

338 foraminiferal calcite traced through the distribution of N, S, and I measured with

339 nanosims: A new challenge for element-ratio-based paleoproxies? Front. Earth Sci. 7, 1–

340 14. https://doi.org/10.3389/feart.2019.00175

341 Grindlay, G., Mora, J., de Loos-Vollebregt, M., Vanhaecke, F., 2013. A systematic study on

342 the influence of carbon on the behavior of hard-to-ionize elements in inductively coupled

343 plasma–mass spectrometry. Spectrochim. Acta Part B At. Spectrosc. 86, 42–49.

344 https://doi.org/10.1016/j.sab.2013.05.002

345 Hardisty, D.S., Horner, T.J., Evans, N., Moriyasu, R., Babbin, A.R., Wankel, S.D., Moffett,

346 J.W., Nielsen, S.G., 2021. Limited iodate reduction in shipboard seawater incubations

347 from the Eastern Tropical North Pacific oxygen deficient zone. Earth Planet. Sci. Lett.

348 554, 116676. https://doi.org/10.1016/j.epsl.2020.116676

349 Hardisty, D.S., Horner, T.J., Wankel, S.D., Blusztajn, J., Nielsen, S.G., 2020. Experimental

350 observations of marine iodide oxidation using a novel sparge-interface MC-ICP-MS

351 technique. Chem. Geol. 532, 119360. https://doi.org/10.1016/j.chemgeo.2019.119360

352 He, T., Dal Corso, J., Newton, R.J., Wignall, P.B., Mills, B.J.W., Todaro, S., Di Stefano, P.,

353 Turner, E.C., Jamieson, R.A., Randazzo, V., Rigo, M., Jones, R.E., Dunhill, A.M., 2020.

354 An enormous sulfur isotope excursion indicates marine anoxia during the end-Triassic

355 mass extinction. Sci. Adv. 6, eabb6704. https://doi.org/10.1126/sciadv.abb6704

356 He, T., Wignall, P.B., Newton, R.J., Atkinson, J.W., Keeling, J.F.J., Xiong, Y., Poulton, S.W.,

357 2022. Extensive marine anoxia in the European epicontinental sea during the end-Triassic

358 mass extinction. Glob. Planet. Change in revision.

359 Hoogakker, B.A.A., Lu, Z., Umling, N., Jones, L., Zhou, X., Rickaby, R.E.M., Thunell, R.,

360 Cartapanis, O., Galbraith, E., 2018. Glacial expansion of oxygen-depleted seawater in the

361 eastern tropical Pacific. Nature 562, 410–413. https://doi.org/10.1038/s41586-018-0589-x

362 Jaraula, C.M.B., Grice, K., Twitchett, R.J., Böttcher, M.E., LeMetayer, P., Dastidar, A.G.,

363 Opazo, L.F., 2013. Elevated pCO$_2$ leading to Late Triassic extinction, persistent photic

zone euxinia, and rising sea levels. Geology 41, 955–958.

https://doi.org/10.1130/G34183.1

Jenkyns, H.C., 2010. Geochemistry of oceanic anoxic events. Geochemistry, Geophys.

Geosystems 11, 1–30. https://doi.org/10.1029/2009GC002788

Jost, A.B., Bachan, A., van de Schootbrugge, B., Lau, K. V., Weaver, K.L., Maher, K., Payne,

J.L., 2017. Uranium isotope evidence for an expansion of marine anoxia during the end-

Triassic extinction. Geochemistry, Geophys. Geosystems 18, 3093–3108.

https://doi.org/10.1002/2017GC006941

Kipp, M.A., Tissot, F.L.H., 2022. Inverse methods for consistent quantification of seafloor

anoxia using uranium isotope data from marine sediments. Earth Planet. Sci. Lett. 577,

117240. https://doi.org/10.1016/j.epsl.2021.117240

Lu, W., Dickson, A.J., Thomas, E., Rickaby, R.E.M., Chapman, P., Lu, Z., 2020. Refining the

planktic foraminiferal I/Ca proxy: Results from the Southeast Atlantic Ocean. Geochim.

Cosmochim. Acta 287, 318–327. https://doi.org/10.1016/j.gca.2019.10.025

Lu, W., Ridgwell, A., Thomas, E., Hardisty, D.S., Luo, G., Algeo, T.J., Saltzman, M.R., Gill,

B.C., Shen, Y., Ling, H., Edwards, C.T., Whalen, M.T., Zhou, X., Gutchess, K.M., Jin,

L., Rickaby, R.E.M., Jenkyns, H.C., Lyons, T.W., Lenton, T.M., Kump, L.R., Lu, Z.,

2018. Late inception of a resiliently oxygenated upper ocean. Science. 5372, eaar5372.

https://doi.org/10.1126/science.aar5372

Lu, Z., Jenkyns, H.C., Rickaby, R.E.M., 2010. Iodine to calcium ratios in marine carbonate as

a paleo-redox proxy during oceanic anoxic events. Geology 38, 1107–1110.

https://doi.org/10.1130/G31145.1

Luo, G., Richoz, S., van de Schootbrugge, B., Algeo, T.J., Xie, S., Ono, S., Summons, R.E.,

2018. Multiple sulfur-isotopic evidence for a shallowly stratified ocean following the

Triassic-Jurassic boundary mass extinction. Geochim. Cosmochim. Acta 231, 73–87.

https://doi.org/10.1016/j.gca.2018.04.015

Luther, G.W., Campbell, T., 1991. Iodine speciation in the water column of the Black Sea.

Deep Sea Res. Part A. Oceanogr. Res. Pap. 38, S875–S882.

https://doi.org/10.1016/S0198-0149(10)80014-7

Oschlies, A., 2021. A committed fourfold increase in ocean oxygen loss. Nat. Commun. 12,

2307. https://doi.org/10.1038/s41467-021-22584-4

Owens, J.D., Lyons, T.W., Hardisty, D.S., Lowery, C.M., Lu, Z., Lee, B., Jenkyns, H.C.,

2017. Patterns of local and global redox variability during the Cenomanian–Turonian

Boundary Event (Oceanic Anoxic Event 2) recorded in carbonates and shales from

central Italy. Sedimentology 64, 168–185. https://doi.org/10.1111/sed.12352

Podder, J., Lin, J., Sun, W., Botis, S.M., Tse, J., Chen, N., Hu, Y., Li, D., Seaman, J., Pan, Y.,

2017. Iodate in calcite and vaterite: Insights from synchrotron X-ray absorption
spectroscopy and first-principles calculations. Geochim. Cosmochim. Acta 198, 218–228.
https://doi.org/10.1016/j.gca.2016.11.032

Pohl, A., Lu, Z., Lu, W., Stockey, R.G., Elrick, M., Li, M., Desrochers, A., Shen, Y., He, R.,
Finnegan, S., Ridgwell, A., 2021. Vertical decoupling in Late Ordovician anoxia due to
reorganization of ocean circulation. Nat. Geosci. 14, 868–873.
https://doi.org/10.1038/s41561-021-00843-9

Rue, E.L., Smith, G.J., Cutter, G.A., Bruland, K.W., 1997. The response of trace element
redox couples to suboxic conditions in the water column. Deep Sea Res. Part I Oceanogr.
Res. Pap. 44, 113–134. https://doi.org/10.1016/S0967-0637(96)00088-X

Ruhl, M., Bonis, N.R., Reichart, G.-J., Damsté, J.S.S., Kürschner, W.M., 2011. Atmospheric
Carbon Injection Linked to End-Triassic Mass Extinction. Science. 333, 430–434.
https://doi.org/10.1126/science.1204255

Song, Haijun, Kemp, D.B., Tian, L., Chu, D., Song, Huyue, Dai, X., 2021. Thresholds of
temperature change for mass extinctions. Nat. Commun. 12, 4694.
https://doi.org/10.1038/s41467-021-25019-2

Todaro, S., Di Stefano, P., Zarcone, G., Randazzo, V., 2017. Facies stacking and extinctions
across the Triassic–Jurassic boundary in a peritidal succession from western Sicily.
Facies 63, 20. https://doi.org/10.1007/s10347-017-0500-5

Todaro, S., Rigo, M., Randazzo, V., Di Stefano, P., 2018. The end-Triassic mass extinction: A
new correlation between extinction events and δ^{13}C fluctuations from a Triassic-Jurassic
peritidal succession in western Sicily. Sediment. Geol. 368, 105–113.
https://doi.org/10.1016/j.sedgeo.2018.03.008

Wignall, P.B., Atkinson, J.W., 2020. A two-phase end-Triassic mass extinction. Earth-Science
Rev. 208, 103282. https://doi.org/10.1016/j.earscirev.2020.103282

Wignall, P.B., Bond, D.P.G., Kuwahara, K., Kakuwa, Y., Newton, R.J., Poulton, S.W., 2010.
An 80 million year oceanic redox history from Permian to Jurassic pelagic sediments of
the Mino-Tamba terrane, SW Japan, and the origin of four mass extinctions. Glob.
Planet. Change 71, 109–123. https://doi.org/10.1016/j.gloplacha.2010.01.022

Zhou, X., Thomas, E., Rickaby, R.E.M., Winguth, A.M.E., Lu, Z., 2014. I/Ca evidence for
upper ocean deoxygenation during the PETM. Paleoceanography 29, 964–975.
https://doi.org/10.1002/2014PA002702

Zhou, X., Thomas, E., Winguth, A.M.E., Ridgwell, A., Scher, H., Hoogakker, B.A.A.,
Rickaby, R.E.M., Lu, Z., 2016. Expanded oxygen minimum zones during the late
Paleocene-early Eocene: Hints from multiproxy comparison and ocean modeling.
Paleoceanography 31, 1532–1546. https://doi.org/10.1002/2016PA003020